Distribution of multiphase fluids in porous media: Comparison between lattice Boltzmann modeling and micro-x-ray tomography

Michael C. Sukop,[1] Haibo Huang,[1] Chen Luh Lin,[2] Milind D. Deo,[3] Kyeongseok Oh,[3] and Jan D. Miller[2]
[1]*Department of Earth Sciences, Florida International University, Miami, Florida 33199, USA*
[2]*Department of Metallurgical Engineering, University of Utah, Salt Lake City, Utah 84112, USA*
[3]*Department of Chemical Engineering, University of Utah, Salt Lake City, Utah 84112, USA*
(Received 3 October 2007; published 27 February 2008)

A parallel implementation of the three-dimensional Shan-and-Chen multicomponent, multiphase lattice Boltzmann method (LBM) was used to simulate the equilibrium distributions of two immiscible fluids in porous media. The simulations were successfully validated against cone-beam x-ray microtomographic data on the distribution of oil (decane), water, and air phases in a 5-mm cube of porous medium composed of packed quartz sand grains. The results confirm that LBM models allow for the straightforward incorporation of complex pore space geometry determined from x-ray microtomography measurements and that simulated wetting and nonwetting phase distributions are consistent with x-ray observations on both macroscopic and microscopic scales.

DOI: 10.1103/PhysRevE.77.026710 PACS number(s): 47.11.−j, 47.55.−t, 47.56.+r, 02.70.−c

I. INTRODUCTION

Multiphase fluid flow in porous media occurs in many environmental and industrial processes, including for example, unsaturated soils, aquifers contaminated with nonaqueous phase liquids, oil recovery, and heap leaching. The lattice Boltzmann (LB) method, which is based on mesoscopic kinetic equations, has been successfully applied to the study of multiphase fluid flow in porous media [1].

We can investigate multiphase fluid flow in porous media using the Shan-and-Chen (SC) LB model, the free-energy-based LB model [2], or a color-gradient-based LB model [3,4]. Among these, the SC multiphase model [5–9] is one of the simplest available multiphase LBMs and, in the form used here, is based on a hydrophobic interaction between fluid phases and additional interaction between the fluids and solid surfaces. It is capable of simulating the complete range of contact angles [10] and the equilibrium distributions of phases in a porous medium as we demonstrate here. The SC LB method can also simulate "single component" multiphase systems that represent a liquid and its own vapor [5,7], but we do not consider that capability further here.

There are numerous studies on multiphase fluids in porous media based on the SC model, but direct validation of model results against pore-scale observations of fluid distributions appears to be rare. For example, Pan *et al.* [11] simulated multiphase fluid flow in a packed sphere system. Good agreement was achieved between the LB simulations and the measured hysteretic capillary pressure-saturation relations. Li *et al.* [12] and Hazlett *et al.* [13] investigated the relative permeabilities for multiphase flow in porous media and the numerical results were qualitatively consistent with experimental observations [12]. Schaap *et al.* [9] have applied the SC model to simulate the imbibition and drainage processes in a microtomographic data set of $405\times405\times100$ voxels, which represent a porous disc with a diameter of 7 mm and a height of 1.7 mm. In their study, a water-Soltrol system and a water-air system are simulated. Although LBM results of wetting and nonwetting phase configurations in orthogonal cross sections in the imbibition and drainage processes are given, they were not compared with x-ray data directly and most of the study is focused on the pressure-saturation characteristics. Coles *et al.* [14] simulated the drainage process in a 6-mm-height and one-inch-diameter core sample using an

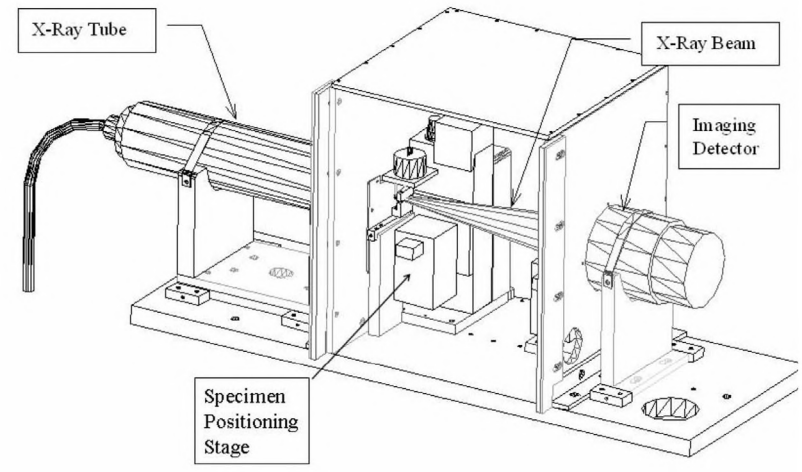

FIG. 1. Cone-beam x-ray microtomography system at the University of Utah.

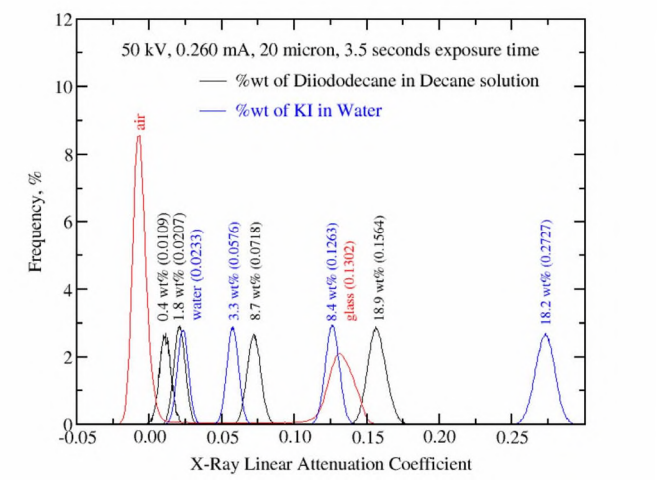

FIG. 2. (Color online) Histograms of x-ray linear attenuation coefficient for different concentrations of KI and diiododecane in water and decane solution, respectively.

SC model and made a direct comparison with observed oil and water distribution in the sample slice by slice. The data were obtained using synchrotron radiation and provided a resolution of 30 μm.

In this paper, we first briefly review the microtomographic methods. Then we use 3D, parallel, Shan-and-Chen-type, multicomponent, multiphase LBM as described in [10] for example, with fluid-surface adhesion proposed in [15], to simulate the configurations of multiphase fluids in a porous medium structure obtained from microtomography measurements. We implement all of our parallel LBM simulations on the MAIDROC Laboratory supercomputer, "Tesla-128," located at the Florida International University Engineering Center campus. In the experiment, the sand was initially water saturated and the water was subsequently displaced by oil. The simulation results are compared with cone-beam x-ray microtomographic data on the distribution of oil (decane), water, and air phases collected at the University of Utah's CT laboratory facility. The comparison of phase distributions is done at both macroscopic (relative saturations by plane through the sample) and microscopic (within-pore phase distributions) scales.

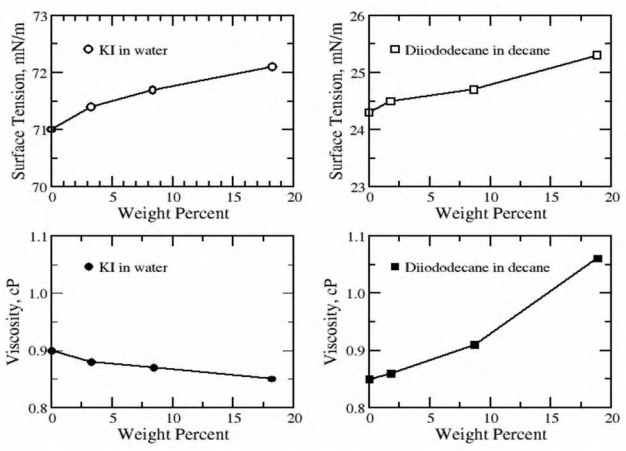

FIG. 3. Effects of KI and diiododecane on physical properties of liquids used in x-ray microtomographic measurements.

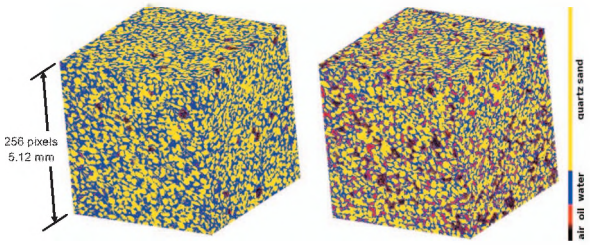

FIG. 4. (Color) X-ray microtomographic data sets $256\times256\times256$, 20 μm/pixel resolution. Initial water-saturated experimental condition on left. Right image shows same sample following displacement of water by decane. (Operating parameters: 50 kV, 0.26 mA, exposure time 3.5 s, 500 views)

II. MICROTOMOGRAPHY EXPERIMENTAL METHODS

Imaging of fluid phase distribution in porous media is essential to developing a better understanding of residual saturations and relative permeabilities. A large number of imaging studies of different displacement processes have been conducted in oil and gas production applications using medical CAT (Computer Assisted Tomography) machines. Only a few high-resolution imaging studies appear to have been conducted using synchrotron x-ray microtomography [14,16,17]. The application of computed tomography (CT) principles at the microscale level, or micro CT, allows for the quantitative investigation of multiphase systems at the micron level in three dimensions. A high-resolution cone-beam microtomography system, installed at the University of Utah, was used for this study [18]. Figure 1 shows a schematic of the cone-beam x-ray microtomography system. This microtomography system has been specifically designed to address

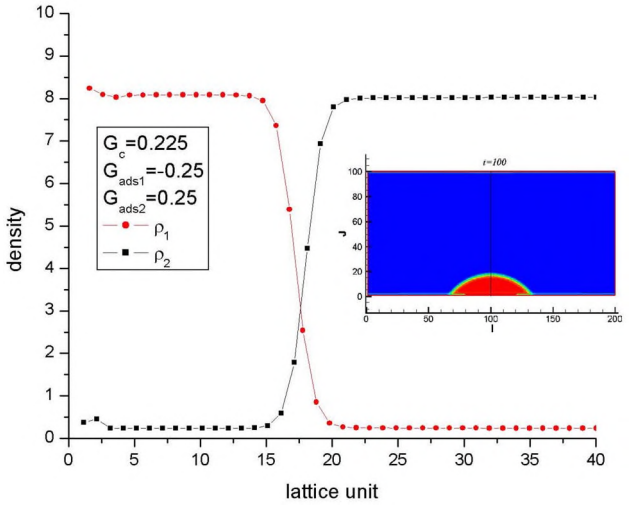

FIG. 5. (Color online) Typical density profiles. The density profile is along the line $i=100$ in a LBM contact angle simulation in a 200 by 100 l.u. simulation as shown on the inset.

the goal of obtaining a 2074×2048 reconstruction over a 10-mm diameter, while at the same time allowing for the imaging of somewhat larger objects (40 mm in diameter). More importantly, the system is designed to be capable of handling high-density samples ($\rho \sim 5$ to 8 g/cm^3).

The 3D x-ray tomographic reconstruction produces a three-dimensional map of x-ray attenuation coefficients of the irradiated specimen. Differentiation of features within the sample is possible because the linear attenuation coefficient (μ) at each point depends directly on the electron density, the effective atomic number (Z) of the material comprising the sample at that point, and the energy of the x-ray beam (E). A simplified equation that illustrates the approximate relationship among these quantities is

$$\mu = \rho\left(a + \frac{bZ^{3.8}}{E^{3.2}}\right), \tag{1}$$

where ρ is the density of the material at a specific point, a is a quantity with a relatively small energy dependence, and b is a constant [19,20]. When a mixture of atomic species is present, Z (the effective atomic number) is defined by

$$Z^{3.8} = \sum_i (f_i[Z_i]^{3.8}), \tag{2}$$

where f_i is the fraction of the total number of electrons contributed by element i with atomic number Z_i.

In this study, immiscible fluid displacement experiments were performed to establish the nature of residual saturations for different fluids flowing in a variety of porous media under different wettability conditions. The magnitude of residual saturation and its structure in the porous medium was directly imaged using microtomography. One of the experiments was conducted using 10-mm diameter sand packs. The displacements began with the packed quartz sand particles saturated fully with water followed by displacement with the oil phase (decane). The packed sand sample was isolated at definite times during displacement and imaged using the microtmography system. Density contrast between the two fluids was achieved by doping both fluids with a high-density "tracers": potassium iodide (KI) and diiododecane were used to enhance x-ray contrast of water and decane phases, respectively. Figure 2 shows the histogram of x-ray attenuation coefficients for different concentrations of KI and diiododecane in water and decane solution, respectively. Based on this calibration, 4.30 wt % of KI in water and 5.45 wt % of diiododecane in decane solution were selected to enhance the contrast of water and decane phases for the displacement study. The x-ray linear attenuation coefficients are about 0.075 and 0.05 for the enhanced water and decane solutions, respectively.

III. RESULTS AND DISCUSSION

A. X-ray microtomography data sets

In the experiment, the sand was initially water saturated and the water was subsequently displaced by oil. As mentioned previously, potassium iodide (KI) and diiododecane were used to enhance x-ray contrast for water and decane fluid phases. These additives have only minor impacts on some of the physical properties of the oil and water at the concentrations employed (Fig. 3). The effect of the additives on the contact angle in the water-decane-quartz system was not tested.

The initial water-saturated experimental condition as measured by x-ray microtomography is shown on the left of Fig. 4. The experimental volume is a cube 5.12 mm on a side. There are minor amounts of trapped air in the sample. The right image in Fig. 4 shows the same sample following displacement of the water by decane. The sample was subsequently flushed with water, but we focus our simulations on the conditions after the decane was introduced.

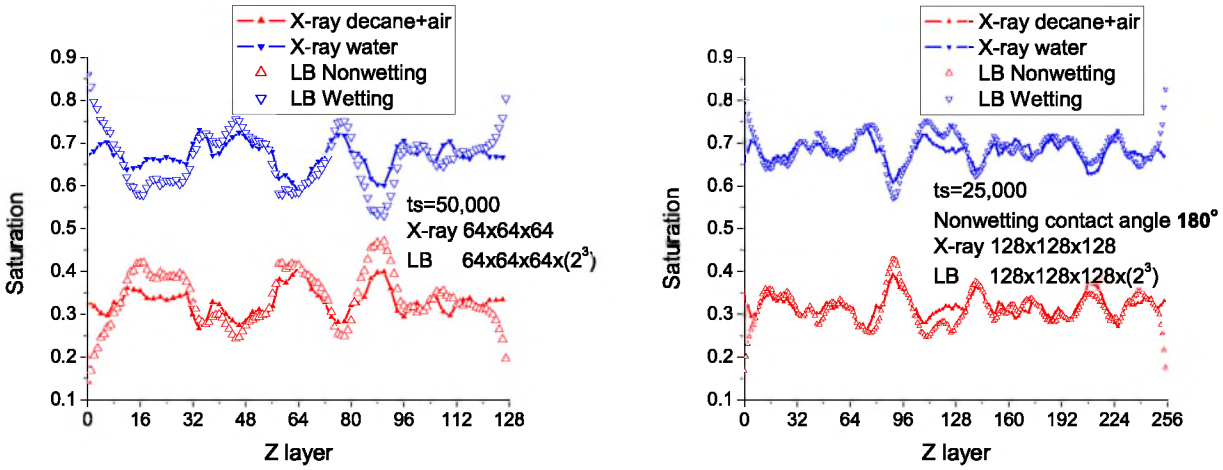

FIG. 6. (Color online) Slice-wise comparison of observed and simulated wetting and nonwetting fluid saturations. Nonwetting fluid contact angle is 180 degrees. The simulations were initialized with the saturation of non-wetting fluid (decane+air) 0.330 and 0.319 for $64 \times 64 \times 64 \times (2^3)$ and $128 \times 128 \times 128 \times (2^3)$ l.u.^{3} respectively, which was calculated from x-ray microtomography data sets.

B. Simulations

A three-dimensional, parallel, Shan-Chen-type, multicomponent, multiphase LBM that is described in more detail in [10], is used to simulate the configurations of the fluids. The parameters that control the contact angle are selected according to Eq. (8) of [10].

1. Partial data sets

First, we performed simulations for small (64^3 voxels) and large (128^3 voxels) data sets, which are one corner of the whole data set and one-eighth of the total 256^3 sample. The porosities of the above two data sets are measured based on the quartz volume (from x-ray data) and total volumes as 0.464 and 0.451, respectively. The x-ray data may indicate the presence of small pores as single voxels. Because the simulated interface thickness may occupy several lattice units, we doubled the side length in each slice (by replacing each pixel by 4 pixels) and duplicated each slice; in that way, we constructed 128^3 and 256^3 voxel porous media to represent the 64^3 and 128^3 data sets respectively for our LBM simulations. Thus the simulation resolution is 10 μm while the data are at 20 μm. This allows the simulations to more realistically reproduce the fluid physics and show smoother interfaces. Even more voxels would be desirable, but may not be justified by the resolution of the x-ray data and the computational cost can become prohibitive. It should be noted that the x-ray data are similarly affected by the limited resolution and jagged fluid-fluid interfaces are sometimes the result (e.g., left side panels of Fig. 7).

In these simulations, we begin with a random distribution of oil and water in the pore space that is constrained to match the observed oil/water volumetric ratios present in the entire sample. Air is a nonwetting fluid and is lumped with decane for the purposes of the simulations. For the large and small cases, we begin with a fine-scale random fluid distribution (Fig. 7) with the saturation of nonwetting fluid (decane +air) 0.330 and 0.319, respectively, based on the bulk saturations obtained from the x-ray data. Endeavoring to compare this approach with the x-ray data entails the assumption that the experimental system approaches an equilibrium distribution of the phases. This seems reasonable given the expected good connectivity of the pore network in this system. In all of the regions occupied by wetting or nonwetting fluid, the fluids have initial density 8.0 and initial complementary density 0.24. We set parameters as $G_c=0.225$, $G_{ads1}=0.45$, and $G_{ads2}=-0.45$; according to Eq. (8) of [10], these parameter choices give a 180° contact angle for the nonwetting fluid (fluid 1) and a 0° contact angle for the wetting fluid (fluid 2). In our simulations, periodic boundaries were set on all sides of the domain and we ran more than 25 000 time steps to achieve equilibration. In [9], methods to estimate the real time represented by the lattice time steps are provided, but our principal concern here is that we reach an equilibrium adequately consistent with the experimental data to justify our assumptions and permit the comparison.

An important issue in our study is how to judge when a lattice node is occupied by nonwetting fluid or wetting fluid so as to calculate the nonwetting or wetting saturation in the pore space. Figure 5 illustrates a typical density profile through a drop on a surface and the surrounding fluid. The density profiles of the two components are not symmetric in the interfacial area as has been observed by Hou *et al.* [8]. However, it is reasonable to set a cutoff such that a lattice node can be regarded as occupied by the nonwetting fluid

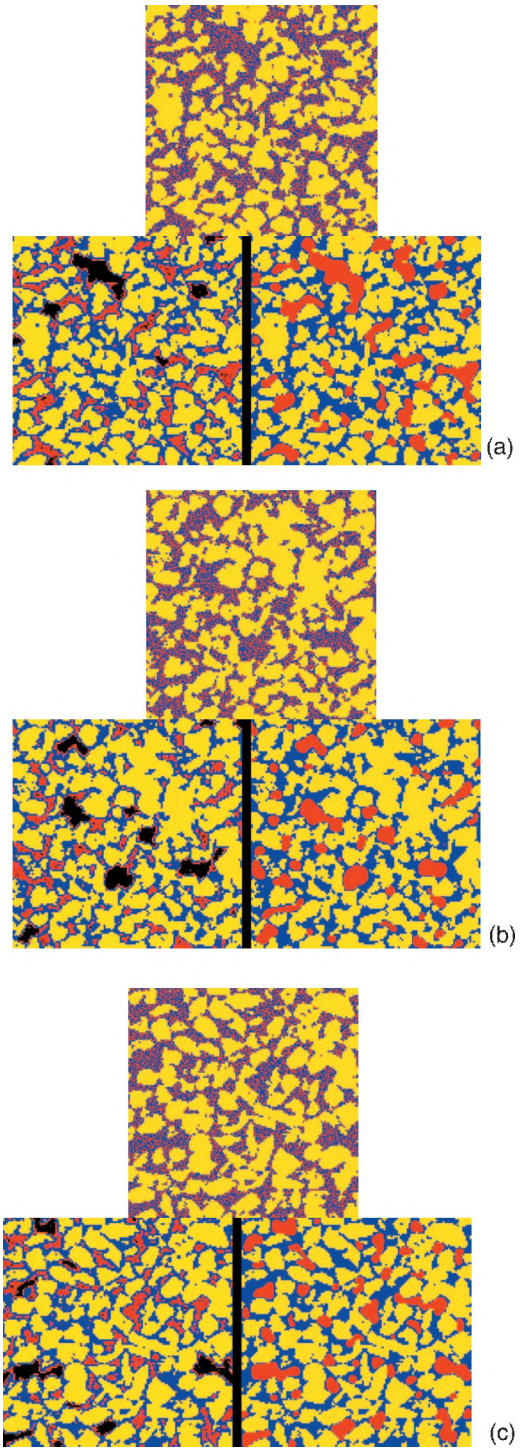

FIG. 7. (Color) Slice (a) $z=64$, (b) $z=128$, and (c) $z=192$ initial conditions (top) and comparison of observed (bottom left) and simulated (bottom right) wetting and nonwetting phase configurations for $256\times256\times256$ case. (Legend: black=air; red=decane; blue=water).

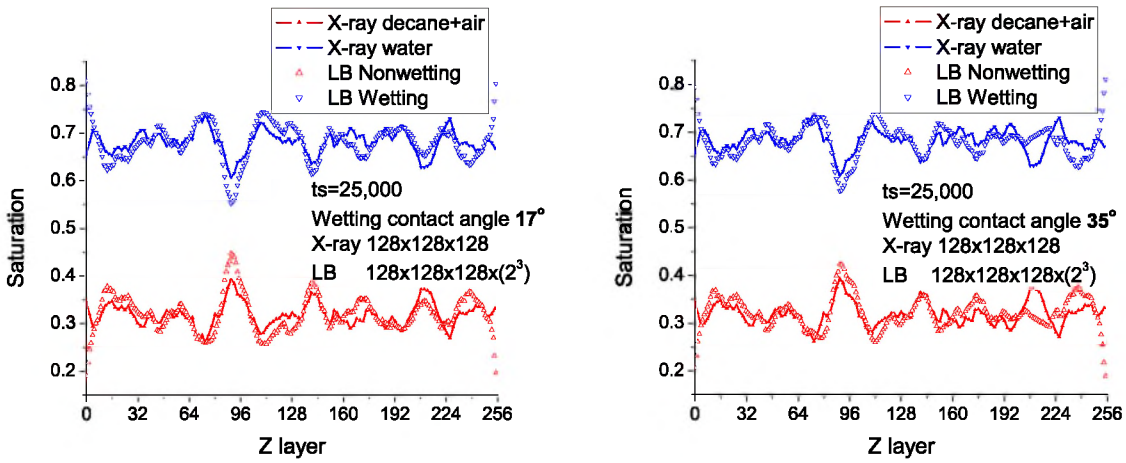

FIG. 8. (Color online) Cases with different contact angle lead to slight differences between LB simulations and experimental results.

when $\rho_{nonwetting} > \rho_{wetting}$ and vice versa. Hereafter, we used this criterion to calculate the saturations.

As equilibrium was attained, the phases redistributed within the pore space. From Fig. 6 we can see that in both cases, the observed slice-wise macroscopic phase saturations obtained from the x-ray data agree well with LB simulations. Compared with the x-ray microtomography data sets, results of the large sample (256^3) simulation are better than the small sample (128^3) simulation. However, the large sample simulation still has small discrepancies with the phase saturations obtained from our experiment. For example, around $z=110$, the wetting phase saturation is a few percent too high. In addition, the simulation results at the boundaries of the sample are not consistent with the x-ray data, but this is not unexpected because the simulation periodic boundaries are unrealistic.

The equilibrium distribution of phases within the pore space in slices at (a) $z=64$, (b) $z=128$, (c) $z=192$ in the LBM 256^3 simulation can be compared in detail with the observed distribution of wetting (blue=water) and nonwetting fluids (black=air; red=decane) in our experiment in Fig. 7. The images on the bottom left are experimental x-ray data while the images on the bottom right are LB simulations. We can see that the simulated phase distributions within the pore space match the observed phase configurations quite well, though in these slices, the model appears to miss some small regions of nonwetting fluid. This is consistent with the small deviations from the macroscopic saturations shown in Fig. 6 and could be due in part to our simulation strategy. It is well known that the injection pressure will control the size of pores invaded by nonwetting fluid. Pressures were not recorded during the decane injection however, and we used the random initial phase distributions based on the bulk saturations as an alternative to injecting the nonwetting fluid in the simulations. Considering that no parameters were adjusted to achieve these results, the agreement between the simulations and the measurements is quite satisfying and adequate for many purposes in our opinion.

LBM models use only parameters related to the fundamental processes being simulated. Since this system is not experiencing flow after equilibration, the viscosities of the phases are largely irrelevant, though they could be critical under other circumstances. Similarly, we believe that when interface configurations and fluid distributions are our sole interest and the Bond number is such that capillary forces dominate over gravity, the absolute and relative densities of the fluids are of no concern. The fluid-fluid interfacial tension is determined by G_c, and the difference between $G_{ads,1}$ and $G_{ads,2}$ relative to G_c determines the contact angle via Eq. (8) of [10]. Thus these model parameters combine to determine the sole remaining potentially key variable, the contact angle.

In the decane/water/quartz system, the contact angle of water may not equal exactly 0 degrees as assumed in the simulations described above. To investigate how much varying the contact angle of water from 0 degrees would affect the simulation results, we carried out some further simulations of phase redistribution with wetting contact angles of 17 and 35 degrees. Figure 8 illustrates the slice-wise comparison of observed and simulated macroscopic wetting and nonwetting fluid saturations when wetting contact angles are 17 and 35 degrees. It is obvious that for the two cases, in some regions—for example, the slices near $z=110$—the simulated phase saturations agree better than when the wetting contact angle is 0, while in other regions (near slice $z=240$ for example), the agreement is worse. We calculated the overall error between the simulated and observed wetting and nonwetting fluid saturations for all three simulated contact angles and found that on the whole, agreement of observed and simulated phase saturation is best when the wetting contact angle is 0 degrees.

2. Complete data set

Finally, we discuss the simulation of the phase redistribution in the entire data set (256^3 voxels). Here for the same reason and using the same method as in the previous cases, we constructed a 512^3 voxel porous medium for our LBM simulations. The porosity of the data set is based on the measured quartz volume (from x-ray data) and total volumes

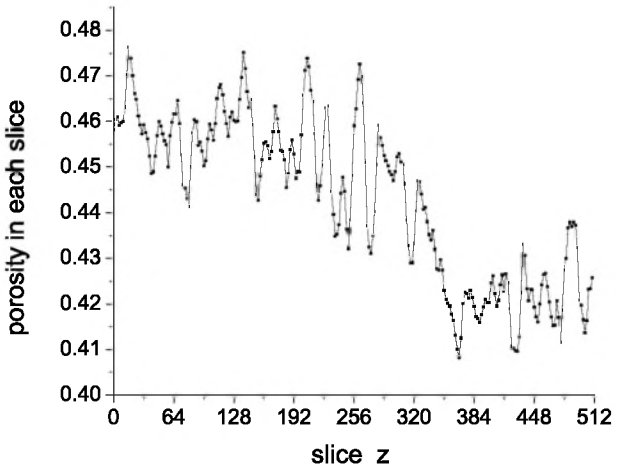

FIG. 9. Observed slice-wise observed porosity in $256\times256\times256$ x-ray microtomography data set. The z value is 2 times the value in the original data set.

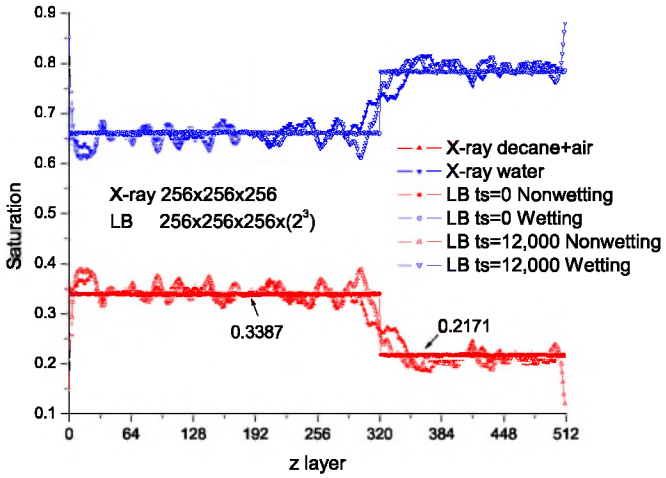

FIG. 10. (Color online) Slice-wise comparison of observed and simulated wetting and nonwetting fluid saturations. Nonwetting fluid contact angle is 180 degrees. The simulations were initialized with the saturation of nonwetting fluid (decane+air) 0.3387 and 0.2171 for slice layers 0–320 and 321–512, respectively, to match the entire nonwetting saturation of 0.295.

is 0.443. However, we observed that there was a rapid change in the slice-wise porosity around $z=320$ (Fig. 9). The reasons for this change in porosity are not known, but it is likely due to variations in grain packing. Beyond slice $z=320$, smaller porosity suggests that the pore size is smaller and it is more difficult for the nonwetting fluid (decane and air) to enter the pore space. For this case, if we begin with a random fluid distribution based on the observed bulk saturation of nonwetting fluid (decane+air) of 0.295, it could take a very long time (perhaps two or three weeks run in a 64 CPU parallel supercomputer) to attain the equilibrium state.

To overcome this difficulty, we used another strategy. We found that the observed slice-wise macroscopic phase saturations obtained from the x-ray data also changed rapidly around slice $z=320$ (Fig. 10). So, in this simulation we initialized the slices $z<320$ with a random fluid distribution based on the observed nonwetting (decane+air) saturation of 0.3387 and initialized at 0.2171 for $z>=320$, as illustrated in Fig. 10.

This way, we attained an equilibrium state very quickly and, after only 12 000 time steps simulation, the LB simulation results agree well with the observed slice-wise macroscopic phase saturations obtained from the x-ray data. However, there are some small discrepancies with the phase saturations obtained from the x-ray measurements, with the greatest differences where the step change in initial saturations was applied.

IV. CONCLUSION

In this paper, multiphase lattice Boltzmann methods were applied to successfully simulate 3D, equilibrium, pore-scale geometric configurations of decane/water distributions measured in a quartz sand porous medium using cone-beam x-ray microtomography. Observed macroscopic phase saturations were also well matched.

The results illustrate the potential of multiphase LBM simulation to describe multiphase fluid distributions in porous media. Future work will focus on dynamic flow systems representative of numerous natural and industrial processes such as flow in unsaturated soils, nonaqueous contamination of aquifers, oil recovery, and heap leaching operations.

ACKNOWLEDGMENTS

We acknowledge support from the Center for Advanced Separation Technologies. Sukop and Huang were supported in part by the National Science Foundation under Grant No. 0440253.

[1] S. Chen and G. D. Doolen, Annu. Rev. Fluid Mech. **30**, 329 (1998).
[2] M. R. Swift, E. Orlandini, W. R. Osborn, and J. M. Yeomans, Phys. Rev. E **54**, 5041 (1996).
[3] J. Tolke, X. Krafczyk, M. Schulz, and E. Rank, Philos. Trans. R. Soc. London, Ser. A **360**, 535 (2002).
[4] M. Latva-Kokko and D. H. Rothman, Phys. Rev. E **72**, 046701 (2005).
[5] X. Shan and H. Chen, Phys. Rev. E **47**, 1815 (1993).
[6] X. Shan and G. Doolen, J. Stat. Phys. **81**, 379 (1995).
[7] J. Hyvaluoma, P. Raiskinmaki, A. Jasberg, A. Koponen, M. Kataja, and J. Timonen, FGCS, Future Gener. Comput. Syst. **20**, 1003 (2004).
[8] S. Hou, X. Shan, Q. Zou, G. D. Doolen, and W. E. Sol, J. Comput. Phys. **138**, 695 (1997).
[9] M. G. Schaap, M. L. Porter, B. S. B. Christensen, and D. Wildenschild, Water Resour. Res. **43**, W12S06 (2007).
[10] H. B. Huang, D. T. Thorne, M. G. Schaap, and M. C. Sukop,

Phys. Rev. E **76**, 066701 (2007).
[11] C. Pan, M. Hilpert, and C. T. Miller, Water Resour. Res. **40**, W01501 (2004).
[12] H. N. Li, C. X. Pan, and C. T. Miller, Phys. Rev. E **72**, 026705 (2005).
[13] R. D. Hazlett, S. Y. Chen, and W. E. Soll, J. Pet. Sci. Eng. **20**, 167 (1998).
[14] M. E. Coles, R. D. Hazlett, P. Spanne, W. E. Soll, E. L. Muegge, and K. W. Jones, J. Pet. Sci. Eng. **19**, 55 (1998).
[15] N. S. Martys and H. D. Chen, Phys. Rev. E **53**, 743 (1996).
[16] K. A. Culligan, D. Wildenschild, B. S. B. Christensen, W. G. Gray, and M. L. Rivers, Adv. Water Resour. **29**, 227 (2006).
[17] B. S. B. Christensen, Ph.D thesis, Technical University of Denmark, 2006 (unpublished).
[18] C. L. Lin and J. D. Miller, Min. Metall. Processing **19**, 65 (2002).
[19] E. C. McCullough, Med. Phys. **2**, 307 (1975).
[20] S. L. Wellington and H. J. Vinegar, JPT, J. Pet. Technol. **39**(8), 885 (1987).